


SCIENTIFIC REPORTS



Corrected: Publisher Correction

OPEN

Tunable long persistent luminescence in the second near-infrared window via crystal field control

Jianmin Nie^{1,2}, Yang Li^{1,3}, Shanshan Liu^{1,2}, Qiuqun Chen^{1,2}, Qi Xu^{1,2} ^{1,2} & Jianrong Qiu^{1,2,4}

Construction of an active composite as a biomarker with deeper tissue penetration and higher signal-to-noise ratio (SNR) is of great importance for the application in bioimaging. Here, we report a strategy for tuning the emission bandwidth and intensity via crystal field control in long persistent phosphors (LPPs). Ni²⁺-doped Zn_{1+y}Sn_yGa_{2-x-2y}O₄ phosphors, with a tunable emission band peaking from 1270 to 1430 nm in the second near-infrared (NIR) window, have been successfully prepared. Such featured materials have the advantages of low absorption and scattering as well as more efficient tissue penetration. The emission spectra can be controlled by tailoring the local crystal field around the activator precisely via substitution of Zn and Sn for Ga. Moreover, with high resolution and weak light disturbance, these developed multi-band afterglow phosphors exhibit great application potential in advanced optical imaging.

In the recent years, biomarkers have become a hot topic and drawn much attention in the application of *in vivo* bioimaging^{1,2}, since high precision and resolution for imaging technology are in great demand. Correspondingly, due to superior performance of long persistent phosphors (LPPs), they are recognized as the suitable materials to satisfy the requirement, i.e. the exclusion of external illumination which removes the possibility of autofluorescence from background noise^{3,4}. Just like other luminescent biomarkers, the applications of LPPs are also strongly dependent on various parameters, including emission bandwidth and intensity. Higher intense afterglow emission and lower transmission loss are essential for improving the signal-to-noise ratio (SNR) in the process of optical signal acquisition in *in vivo* imaging^{5,6}. Indeed, near-infrared (NIR) light can penetrate biological tissues, such as skin and blood, more efficiently than visible light, while the light in the second NIR window (1000–1400 nm) has lower absorption, lower scattering and more efficient tissue penetration than the light in the first NIR window (650–950 nm)^{7,8}. Thus, optical materials with tunable spectra are still highly desirable; especially long persistent phosphors with NIR emission. Unfortunately, an instructive methodology of purposefully tuning the afterglow properties is still missing^{9–12}.

Perfect crystals did not exist in reality. Foreign atoms or imperfections make materials highly interesting in the aspect of functional and structural systems. Therefore, these foreign atoms are either chosen as the optical and electrical activators to offer the anticipative application, or as the purposely introduced dopant to vary the local site symmetry^{13,14}. Hence, we suggest a strategy of element substitution to tune the operational waveband and emission intensity. This route potentially achieves the control of crystal field surrounding the activators and increases the SNR during the process of optical signal acquisition. Experimentally, we demonstrate that the long persistent phosphorescence in Zn_{1+y}Sn_yGa_{2-x-2y}O₄: xNi²⁺ with the tunable emission band peaking from 1270 to 1430 nm is tailored by controlling local crystal field around the activator, which allows extensive control of emission band in the second NIR window.

¹State Key Laboratory of Luminescent Materials and Devices, School of Materials Science and Technology, South China University of Technology, Guangzhou, 510640, China. ²Guangdong Provincial Key Laboratory of Fiber Laser Materials and Applied Techniques, South China University of Technology, Guangzhou, 510640, China. ³School of Physics and Optoelectronic Engineering, Guangdong University of Technology, Guangzhou, 510006, China. ⁴State Key Laboratory of Modern Optical Instrumentation, College of Optical Science and Engineering, Zhejiang University, Hangzhou, Zhejiang, 310027, China. Correspondence and requests for materials should be addressed to Y.L. (email: lychris@sina.com) or J.Q. (email: qjr@scut.edu.cn)

Received: 10 April 2017

Accepted: 8 September 2017

Published online: 29 September 2017

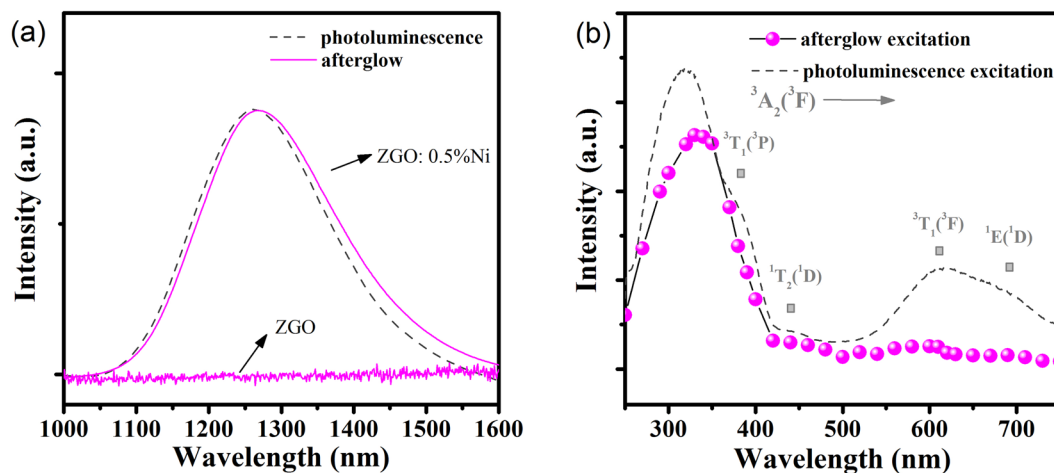


Figure 1. (a) Afterglow spectra of Ni²⁺-doped (ZGO: 0.5%Ni) and non-doped (ZGO) ZnGa₂O₄ phosphors after the irradiation by an ultraviolet lamp for 10 minutes, and photoluminescence spectrum of the ZGO: 0.5%Ni phosphor under excitation at 320 nm. (b) Photoluminescence excitation spectrum and afterglow excitation spectrum of ZGO: 0.5%Ni phosphor monitored at 1270 nm.

Results and Discussion

Long persistent phosphorescence in the second near-infrared window.

As a proof-of-concept experiment, we first synthesized a phosphor with persistent luminescence in the second near-infrared (NIR) window. In Fig. 1(a), non-doped ZnGa₂O₄ (ZGO) phosphor does not show any persistent phosphorescence after the irradiation, while Ni²⁺-doped ZnGa₂O₄ (ZGO: 0.5%Ni) phosphor exhibits a long persistent phosphorescence from 1050 to 1600 nm with peak at 1270 nm, covering a large part of the second NIR window. Also, a similar emission band is shown in the photoluminescence (PL) spectrum of ZGO: 0.5%Ni phosphor, which can be assigned to the ³T₂(³F) → ³A₂(³F) transition of octahedral Ni²⁺ ions¹⁵. ZnGa₂O₄ is a typical AB₂O₄-type spinel crystal. It's more likely that Ni²⁺ ions are incorporated into the octahedral lattice sites, due to its similar ion radius with Ga³⁺ ion and the strong octahedral coordination preference¹⁶. Figure 1(b) shows the photoluminescence excitation (PLE) spectrum of ZGO: 0.5%Ni phosphor. The wavebands at 390 nm and 620 nm should be ascribed to the spin-allowed transitions of Ni²⁺, ³A₂(³F) → ³T₁(³P) and ³A₂(³F) → ³T₁(³F), respectively. Two small shoulders at about 440 nm and 690 nm correspond to the spin-forbidden transitions of Ni²⁺, ³A₂(³F) → ¹T₂(¹D) and ³A₂(³F) → ¹E(¹D), respectively. These characteristic excitation peaks imply the octahedral coordination surrounding divalent nickel in ZGO: 0.5%Ni phosphor^{17,18}. The attribution of ultraviolet excitation band is usually controversial. The strongest peak at 320 nm in ultraviolet region overlaps with Ni²⁺ [³A₂(³F) → ³T₁(³P)] band. To further effectively identify the ultraviolet excitation band, an afterglow excitation spectrum is measured. A distinct afterglow excitation band is shown in Fig. 1(b). It seemingly consists of two PLE peaks at 320 and 390 nm. Therefore, the ultraviolet excitation band at 320 nm should be assigned to the transition between ground state of Ni²⁺ to conduction band (CB), since capturing of an electron through the CB may be the most efficient path for the electron charging process^{19,20}.

Another interesting property of Ni²⁺-doped ZnGa₂O₄ phosphor is the spectra shift of PL (Supplementary Fig. S1) and afterglow band (Fig. 2(a)) as a function of Ni dopant concentration. With the increment of Ni²⁺ doping concentration, a red-shift of emission band is present, and the afterglow intensity first increases and then decreases, as shown in Fig. 2(b). Seemingly, 0.5% doping concentration of Ni²⁺ is suitable relatively. This variation of spectra shift according to the doping content of Ni²⁺ ions may be related to the energy transfer between neighboring Ni²⁺. The X-ray diffraction (XRD) of Ni²⁺-doped ZnGa₂O₄ phosphor is shown in Fig. 2(c), demonstrating that spectra shift has no concern with the crystal structure. To further validate if a possible reason for this phenomenon is because of energy difference between the electronic transitions of Ni²⁺, absorption spectra is often chosen as a tool²¹. In Fig. 2(d), the position of absorption peaks correspond to the transitions of Ni²⁺ in the octahedral sites²². Nevertheless, an overlap between the emission band at shorter wavelength region and the absorption band centered at 1045 nm may lead to the emission shift²³. Because the distance between neighboring Ni²⁺ ions becomes shorter for higher Ni²⁺ concentration, the probability of energy transfer increases. The re-absorption by neighboring Ni²⁺ ions is suitable for elaborating the spectra shift in Fig. 2(a).

Controlling long persistent phosphorescence via crystal field.

The hallmark of transition metal ions is that the electrons in their outmost d orbital strongly interact with their ligands and that the electronic configuration of the activation ions is affected strongly by the arrangement of surrounding ligands¹³. It is possible to control emission band via modulating the local crystal field surrounding Ni²⁺ ions. The radius of Sn⁴⁺ ion is similar as that of Ga³⁺ ion, and Sn⁴⁺ usually adapts to the octahedral configuration with the Sn-O distances (2.055 Å), close to Ga-O distances (1.98 Å), so Tin (Sn) might be a potential structural modifier to ZnGa₂O₄ host. As expected, the tunable PL and afterglow peak from 1270 to 1430 nm is observed in Zn_{1+y}Sn_yGa_{1.995-2y}O₄:0.5% Ni²⁺ (where y = 0.05, 0.1, 0.3, 0.5, 0.7 and 0.9; designated as SZGO1, SZGO2, SZGO3, SZGO4, SZGO5 and SZGO6, respectively) phosphors (Supplementary Fig. S2 and Fig. 3(a)). Figure 3(b) displays the position variation of emission

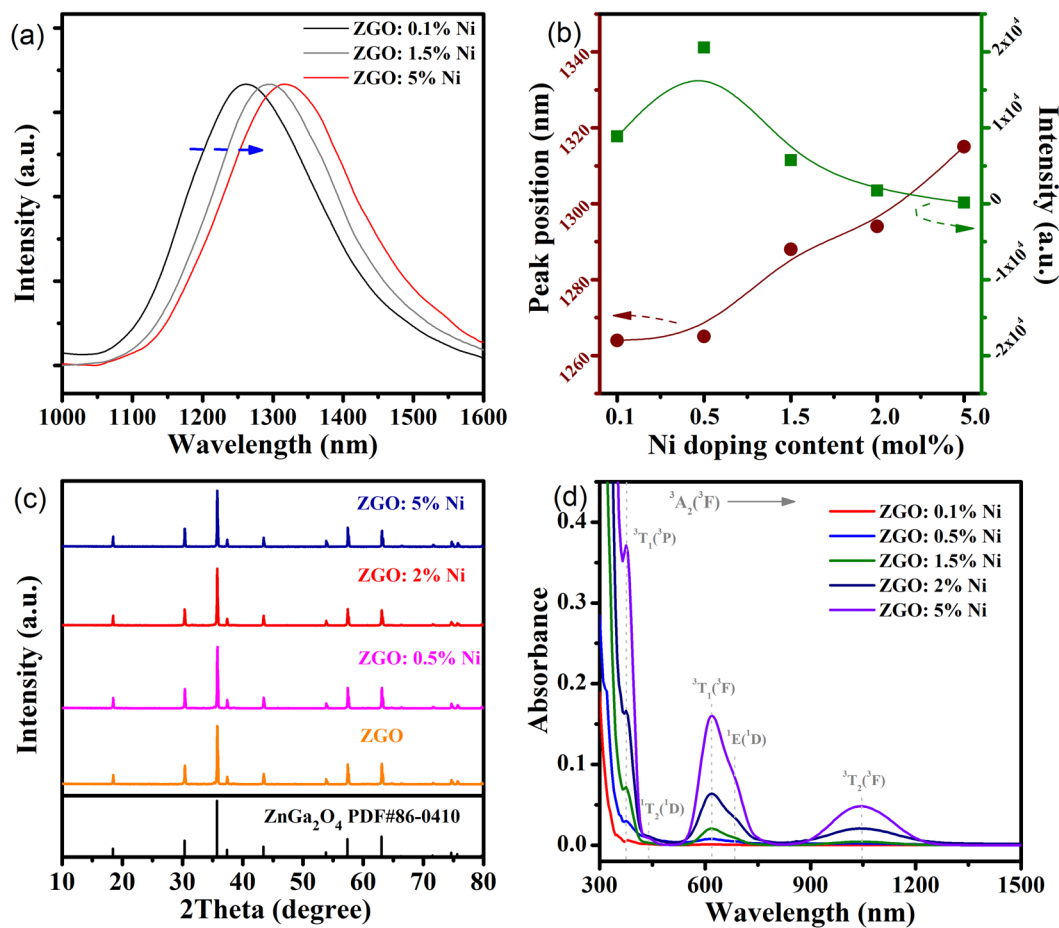


Figure 2. (a) Normalized afterglow spectra of ZGO: $x\text{Ni}^{2+}$ ($x=0.1\%$, 1.5% , 5%) phosphors after the irradiation by an ultraviolet lamp for 10 minutes. (b) Dependence of emission peak position (brown line) and afterglow intensity (green line) on Ni^{2+} doping concentrations. (c) X-ray diffraction patterns of ZGO: $x\text{Ni}^{2+}$ ($x=0\%$, 0.5% , 2% , 5%) phosphors. (d) Absorption spectra of ZGO: $x\text{Ni}^{2+}$ ($x=0.1\%$, 0.5% , 1.5% , 2% , 5%) phosphors.

peak as a function of y value of $\text{Zn}_{1+y}\text{Sn}_y\text{Ga}_{1.995-2y}\text{O}_4:0.5\% \text{Ni}^{2+}$ phosphors: the higher y value achieves, the longer emission wavelength gets. In addition, both the PL and afterglow intensity increase firstly but drop later with increment of y value.

In previous section, we acquire energy level distributions from absorption spectra (Supplementary Fig. S3), which can be applied for calculating the crystal field parameters of Ni^{2+} ions in these phosphors with the help of the Tanabe-Sugano matrix^{24,25}. The crystal field splitting parameter ($10Dq$) and the Racah parameter (B) can be estimated by spectroscopic data from the expression as follows:

$$10Dq = \nu_1 \quad (1)$$

$$B = (\nu_2^2 + 2\nu_2^1 - 3\nu_1\nu_2)/(15\nu_2 - 27\nu_1) \quad (2)$$

where ν_1 and ν_2 are the wavenumbers of absorption bands corresponding to [³A₂(³F) → ³T₂(³F)] and [³A₂(³F) → ³T₁(³P)] transitions of Ni^{2+} ions, respectively. All obtained crystal field parameters are given in Table 1 and Fig. 3(c). Based on the experimental data, the crystal field ($10Dq/B$) is weakened gradually with the higher concentration of Sn and Zn. Lower crystal field contributes to a decreasing in the transition energy from the excited state levels to the ground state level, which is in accordance with the red shift of experimental variation both in spectroscopic data. Zhou *et al.*²⁶ have investigated the infrared-luminescent Ni^{2+} -activated materials with tunable and ultra-broadband luminescent characteristics. In their research, they demonstrated that both the distribution of crystal anions and the size of coordination polyhedrons play an important role in tuning the optical properties of central ion. According to the X-ray diffraction patterns in Fig. 3(d), the diffraction peaks shift to lower angles at higher y value, indicating the lattice expanded gradually because of the formation of solid solution in terms of Bragg's law. An excess of SnO_2 leads to the appearance of an unidentified peak with an asterisk in high Sn substituted sample. The crystal phases of Ni^{2+} -doped $\text{Zn}_{1+y}\text{Sn}_y\text{Ga}_{1.995-2y}\text{O}_4$ phosphors vary from normal spinel to inverse spinel with the increasing of y value²⁷. In Zn_2SnO_4 , an inverse spinel crystal, Zn^{2+} ions are distributed in the octahedral and the tetrahedral sites whereas Sn^{4+} ions occupy octahedral sites. The smaller Ga^{3+} (62 pm)

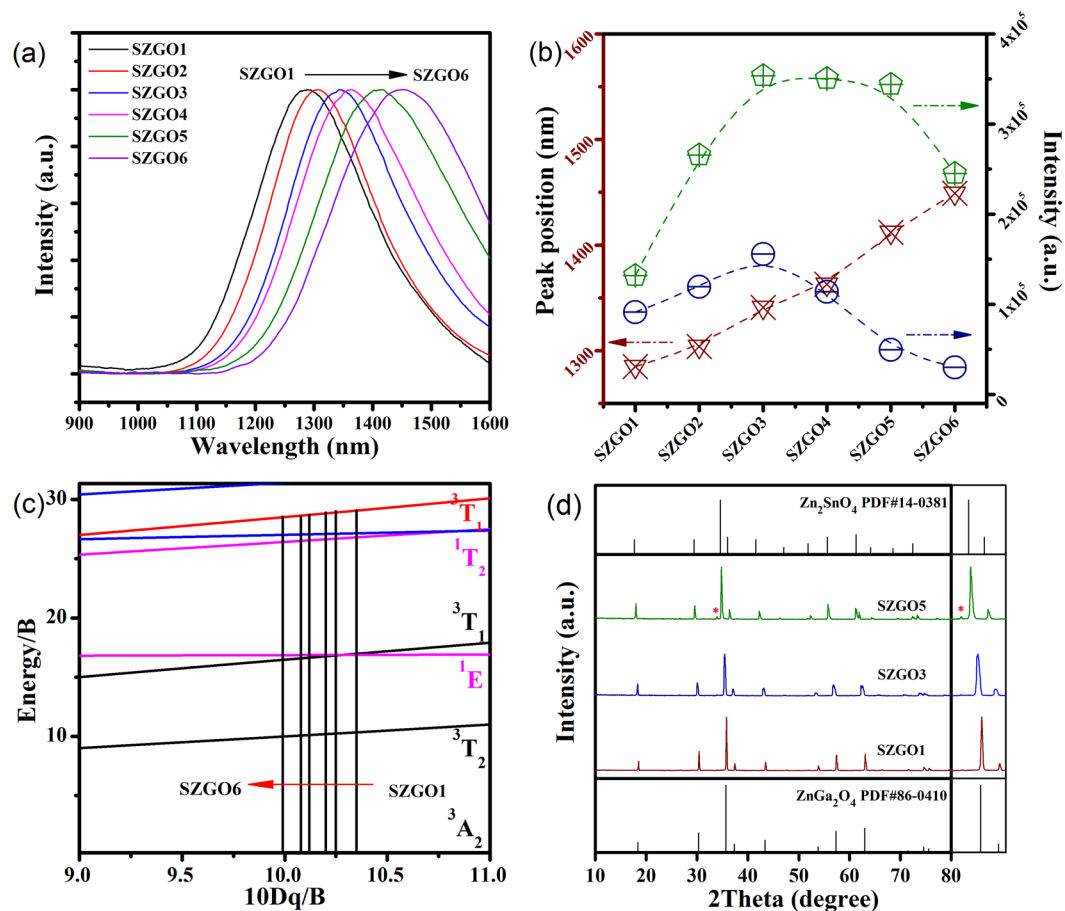


Figure 3. (a) Normalized afterglow spectra of the SZGO1-6 phosphors after the irradiation by an ultraviolet lamp for 10 minutes. (b) Dependence of emission peak positions (brown line), photoluminescence intensity (green line) and afterglow intensity (blue line) on the SZGO1-6 phosphors. (c) Tanabe-Sugano diagram in which the straight lines indicate the normalized crystal field of Ni^{2+} in the SZGO1-6 phosphors. (d) X-ray diffraction patterns of the SZGO1, SZGO3 and SZGO5 phosphors.

Sample	ν_1 [cm^{-1}]	ν_2 [cm^{-1}]	Dq [cm^{-1}]	B [cm^{-1}]	10 Dq/B
SZGO1	9652	27100	965	932	10.35
SZGO2	9560	26954	956	932	10.25
SZGO3	9461	26738	946	927	10.20
SZGO4	9302	26385	930	919	10.12
SZGO5	9116	25907	911	905	10.08
SZGO6	8897	25381	884	890	9.99

Table 1. Estimated crystal field parameters of Ni^{2+} in the $\text{Zn}_{1+y}\text{Sn}_y\text{Ga}_{1.995-2y}\text{O}_4:0.5\% \text{Ni}^{2+}$ (where $y = 0.05, 0.1, 0.3, 0.5, 0.7$ and 0.9 ; designated as SZGO1, SZGO2, SZGO3, SZGO4, SZGO5 and SZGO6, respectively) phosphors. ν_1 and ν_2 are the wavenumbers of absorption bands corresponding to $[^3\text{A}_2(^3\text{F}) \rightarrow ^3\text{T}_2(^3\text{F})]$ and $[^3\text{A}_2(^3\text{F}) \rightarrow ^3\text{T}_1(^3\text{P})]$ transitions of Ni^{2+} ions, respectively. Dq and B mean the crystal field splitting and the Racah parameter²⁵.

ions are substituted by both Sn^{4+} (69 pm) and Zn^{2+} (74 pm) ions, so the $\text{Ni}^{2+}-\text{O}^{2-}$ distance is lengthened and the degree of splitting energy decreases²⁸. As a result, a decrease of energy splitting and a red spectral shift is dependent on the Sn and Zn doping content. Figure 4(a) shows the afterglow decay curves of the SZGO1-6 and ZGO: 0.5%Ni phosphors. The afterglow time increases at the beginning, and then decreases. In general, long persistent phosphorescence is closely associated with the migration of dynamic carrier among trapping states. Electron paramagnetic resonance (EPR) can identify the variation, especially for the unpaired electron^{14,16,29}. The value of g is the primary empirical parameter that characterizes the response of a paramagnetic molecule. A new signal at about $g = 2.18$ appears after the ultraviolet irradiation in the EPR spectra of all Ni^{2+} -doped samples, implying the existence of a number of detectable unpaired electrons (Fig. 4(b) and Supplementary Fig. S6). Meanwhile, this new signal at $g = 2.18$ attenuates after stopping of irradiation, quickly at first, and then slowly with time,

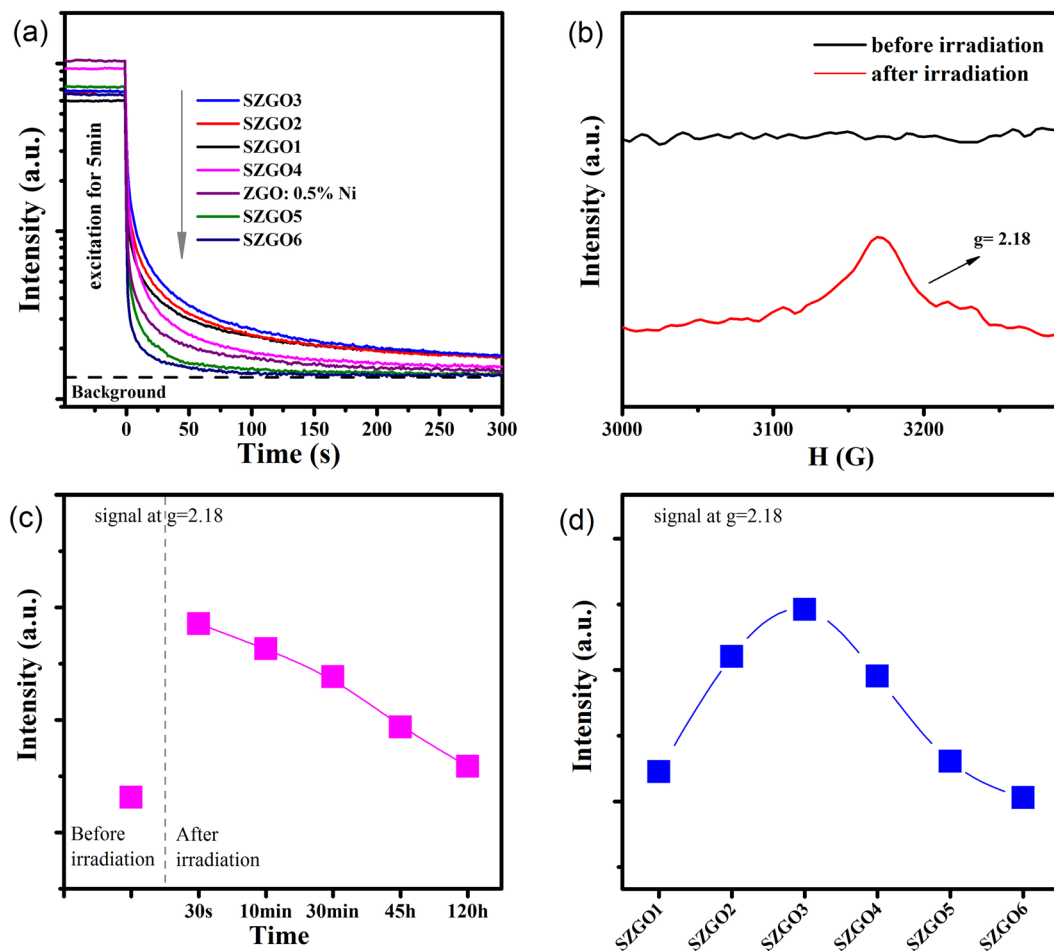


Figure 4. (a) Afterglow decay curves monitored at respective optimized emission wavelength of the SZGO1-6 phosphors and ZGO: 0.5% Ni (at 1270, 1305, 1345, 1365, 1410, 1430 and 1270 nm). All samples were pre-excited at 320 nm by a xenon lamp for 5 minutes. (b) EPR spectra of the SZGO2 phosphor before and after the irradiation by an ultraviolet lamp for 10 minutes. (c) Dependence of the intensity of the signal at $g = 2.18$ on time after ceasing the ultraviolet excitation for the SZGO2 phosphor. (d) Dependence of the intensity of the signal at $g = 2.18$ on the SZGO1-6 phosphors after ceasing the ultraviolet excitation.

which is consistent with the afterglow degradation (Fig. 4(c)). These results may suggest that Ni^{2+} participates in the persistent duration as the trap center^{30,31}. The intensity variation of the signal at $g = 2.18$ of different samples after ceasing the ultraviolet excitation is shown in Fig. 4(d). The result demonstrates that SZGO3 phosphor has a suitable trap structure. As discussed above, with the increasing of Zn and Sn content substitution for Ga in $\text{Zn}_{1+y}\text{Sn}_y\text{Ga}_{1.995-2y}\text{O}_4: 0.5\% \text{Ni}^{2+}$, the crystal field around Ni^{2+} becomes smaller. A larger $\text{Ni}^{2+}-\text{O}^{2-}$ distance along with the lattice expand leads to the tunable persistent phosphorescence in the second NIR window. The persistent duration determined by trapping state has also been affected.

Near-infrared imaging in pork tissues. For a proof-of-concept demonstration of bioimaging, a preliminary NIR-imaging in pork tissue of the SZGO3 phosphor is provided, using a supersensitive camera in dark room (Supplementary Fig. S9). Figure S9(b–e) shows the images taken at the same location at different time intervals. The signal detected from the phosphor could clearly distinguish from autofluorescence of the tissue in real-time observation. The phosphor gives a strong signal at first and then decreases with time. The afterglow signal is detectable for 10 minutes with high resolution in the sensitivity limit of the system measurement. It is shown that this NIR phosphorescent material has the possibility of potentially being applied in advanced bioimaging. However, further research is still underway on nanocrystallization and functionalization of these phosphors.

Conclusions

In summary, we demonstrate $\text{ZnGa}_{2-x}\text{O}_4: x\text{Ni}^{2+}$ and $\text{Zn}_{1+y}\text{Sn}_y\text{Ga}_{2-x-2y}\text{O}_4: x\text{Ni}^{2+}$ long persistent phosphors (LPPs), which feature an emission band from 1050 to 1600 nm in the second near-infrared (NIR) window. By means of increasing Zn and Sn substitution content for Ga, the exceptional peak shift of ultrabroadband NIR persistent phosphorescence can be tuned from 1270 to 1430 nm via controlling the crystal field around Ni^{2+} . Furthermore, the characteristic operational waveband and excellent tunability offer the possibility of these NIR

phosphorescent materials as multifunctional optical materials applying for visualizing structural and functional process in cells, tissues and other complex system.

Methods

Materials. 4 N Pure ZnO, Ga₂O₃, SnO₂ and NiO were selected as raw materials.

Synthesis. Phosphors with molar composition of ZnGa_{2-x}O₄: xNi²⁺ (x = 0, 0.1%, 0.5%, 1%, 1.5%, 2%, 5%) and Zn_{1+y}Sn_yGa_{1.995-2y}O₄: 0.5% Ni²⁺ (y = 0.05, 0.1, 0.3, 0.5, 0.7, 0.9), (Supplementary Table S1) were prepared by conventional high temperature solid state reaction method. The stoichiometric starting materials were thoroughly homogenized by using an agate pestle and mortar for grinding, the mixture was transferred into an alumina crucible and then sintered at 1873 K for 3 hours in air included two heating processes with different heating rates (that is, below 1073 K at 5 K/minutes, from 1073 K to 1873 K at about 3 K/minutes). After that, the samples were furnace-cooled to room temperature and ground again into powder for subsequent use.

Measurements and characterization. The prepared materials were analyzed by X-ray diffraction (XRD) (Cu/Kα) and the data was collected between 10° and 80°. The morphology and particle size of the prepared phosphors were observed by Nova Nano SEM 430 Scanning Electron Microscopy (SEM, Supplementary Fig. S10). Room-temperature photoluminescence (PL) spectra, photoluminescence excitation (PLE) spectra, afterglow spectra and decay curves were measured with a high resolution spectrofluorometer (UK, Edinburgh Instruments, FLS920) equipped with a 500 W xenon lamp as an excitation source, with a Hamamatsu R928P visible photomultiplier (250–850 nm) and a liquid nitrogen-cooled Hamamatsu R5509-72 NIR photomultiplier as the detectors. The afterglow excitation spectra were extracted from afterglow decay curves monitored at 1270 nm after different excitation wavelengths. The phosphor was pre-irradiated for 5 minutes by xenon lamp between 250 nm to 750 nm in 10 nm or 20 nm steps. Subsequently, we took afterglow intensity I_{10s} as a function of the excitation wavelengths over the spectral range of 250–750 nm, I_{10s} means the afterglow intensity recorded at ten seconds after irradiation ended. The absorption spectra were measured by PerkinElmer Lambda 950 spectrometer in the region of 300–1500 nm. Electron paramagnetic resonance (EPR) spectra were recorded by using a Bruker E500 EPR spectrometer operating at X-band microwave frequency for studying paramagnetic defects. The samples were pre-annealed at 773 K for 10 minutes before testing, which were measured both before and after the irradiation by an ultraviolet lamp for 10 minutes.

Imaging. Near-infrared (NIR) persistent luminescent tissue imaging were performed with a modified imaging system, using a Germany Goldeye P-008 NIR camera as the signal collector. The phosphor was spread on the pork tissue at the depth of 3 mm. The used pork with a size of 14 mm × 20 mm × 5 mm was bought from the supermarket. All images were taken in a dark room under the camera exposure time of 1000 milliseconds after excitation by an ultraviolet lamp for 10 minutes, and analyzed with home-made software.

References

- Maldiney, T. *et al.* The *in vivo* activation of persistent nanophosphors for optical imaging of vascularization, tumours and grafted cells. *Nat. Mater.* **13**, 418–426 (2014).
- Abdukayum, A., Chen, J. T., Zhao, Q. & Yan, X. P. Functional Near Infrared-Emitting Cr³⁺/Pr³⁺ Co-Doped Zinc Gallogermanate Persistent Luminescent Nanoparticles with Superlong Afterglow for *in Vivo* Targeted Bioimaging. *J. Am. Chem. Soc.* **135**, 14125–14133 (2013).
- Pan, Z. W., Lu, Y. Y. & Liu, F. Sunlight-activated long-persistent luminescence in the near-infrared from Cr³⁺-doped zinc gallogermanates. *Nat. Mater.* **11**, 58–63 (2012).
- Hong, G. S. *et al.* Through-skull fluorescence imaging of the brain in a new near-infrared window. *Nat. Photonics* **8**, 723–730 (2014).
- Maldiney, T. *et al.* Gadolinium-Doped Persistent Nanophosphors as Versatile Tool for Multimodal *In Vivo* Imaging. *Adv. Funct. Mater.* **25**, 331–338 (2015).
- Hong, G. S. *et al.* *In Vivo* Fluorescence Imaging with Ag₂S Quantum Dots in the Second Near-Infrared Region. *Angew. Chem. Int. Ed.* **51**, 9818–9821 (2012).
- Smith, A. M., Mancini, M. C. & Nie, S. Second window for *in vivo* imaging. *Nat. Nanotechnol.* **4**, 710 (2009).
- Xu, J., Tanabe, S., Sontakke, A. D. & Ueda, J. Near-infrared multi-wavelengths long persistent luminescence of Nd³⁺ ion through persistent energy transfer in Ce³⁺, Cr³⁺ co-doped Y₃Al₂Ga₃O₁₂ for the first and second bio-imaging windows. *Appl. Phys. Lett.* **107**, 4 (2015).
- Li, Y., Gecevicius, M. & Qiu, J. R. Long persistent phosphors—from fundamentals to applications. *Chem. Soc. Rev.* **45**, 2090–2136 (2016).
- Ly, R. C. *et al.* A Yolk-like Multifunctional Platform for Multimodal Imaging and Synergistic Therapy Triggered by a Single Near-Infrared Light. *ACS Nano* **9**, 1630–1647 (2015).
- Wang, Z. B. *et al.* Superlong and Color-Tunable Red Persistent Luminescence and Photostimulated Luminescence Properties of NaCa₂GeO₄F:Mn²⁺, Yb³⁺ Phosphor. *Inorg. Chem.* **55**, 12822–12831 (2016).
- Chen, D. Q., Chen, Y., Lu, H. W. & Ji, Z. G. A Bifunctional Cr/Yb/Tm:Ca₃Ga₂Ge₃O₁₂ Phosphor with Near-Infrared Long-Lasting Phosphorescence and Upconversion Luminescence. *Inorg. Chem.* **53**, 8638–8645 (2014).
- Li, Y. *et al.* Tailoring of the trap distribution and crystal field in Cr³⁺-doped non-gallate phosphors with near-infrared long-persistence phosphorescence. *NPG Asia Mater* **7**, 11 (2015).
- Bessiere, A., Lecointre, A., Priolkar, K. R. & Gourier, D. Role of crystal defects in red long-lasting phosphorescence of CaMgSi₂O₆: Mn diopsides. *J. Mater. Chem.* **22**, 19039–19046 (2012).
- Zhou, S. F. *et al.* Intense infrared luminescence in transparent glass-ceramics containing beta-Ga₂O₃: Ni²⁺ nanocrystals. *J. Phys. Chem. C* **111**, 7335–7338 (2007).
- Bessiere, A. *et al.* Storage of Visible Light for Long-Lasting Phosphorescence in Chromium-Doped Zinc Gallate. *Chem. Mater.* **26**, 1365–1373 (2014).
- Ye, S. Y., Zhang, Y. H., He, H. L., Qiu, J. R. & Dong, G. P. Simultaneous broadband near-infrared emission and magnetic properties of single phase Ni²⁺-doped beta-Ga₂O₃ nanocrystals via mediated phase-controlled synthesis. *J. Mater. Chem. C* **3**, 2886–2896 (2015).
- Liu, F., Liang, Y. J., Chen, Y. F. & Pan, Z. W. Divalent Nickel-Activated Gallate-Based Persistent Phosphors in the Short-Wave Infrared. *Adv. Opt. Mater.* **4**, 562–566 (2016).

19. Bessiere, A. *et al.* ZnGa₂O₄:Cr³⁺: a new red long-lasting phosphor with high brightness. *Opt. Express* **19**, 10131–10137 (2011).
20. Zhuang, Y. X., Ueda, J., Tanabe, S. & Dorenbos, P. Band-gap variation and a self-redox effect induced by compositional deviation in Zn_xGa₂O_{3+x}:Cr³⁺ persistent phosphors. *J. Mater. Chem. C* **2**, 5502–5509 (2014).
21. Tanabe, Y. & Sugano, S. On the absorption spectra of complex ions. I. *J. Phys. Soc. Jpn.* **9**, 753–766 (1954).
22. Suzuki, T., Murugan, G. S. & Ohishi, Y. Optical properties of transparent Li₂O-Ga₂O₃-SiO₂ glass-ceramics embedding Ni-doped nanocrystals. *Appl. Phys. Lett.* **86** (2005).
23. Wu, B. T. *et al.* Optical properties of transparent alkali gallium silicate glass-ceramics containing Ni²⁺-doped beta-Ga₂O₃ nanocrystals. *J. Mater. Res.* **22**, 3410–3414 (2007).
24. Shigemura, H. *et al.* Optical property and local environment of Ni²⁺ in fluoride glasses. *J. Phys. Chem. B* **102**, 1920–1925 (1998).
25. Zhou, S. F. *et al.* Size-induced crystal field parameter change and tunable infrared luminescence in Ni(2+)-doped high-gallium nanocrystals embedded glass ceramics. *Nanotechnology* **19** (2008).
26. Zhou, S. F., Jiang, N., Wu, B. T., Hao, J. H. & Qiu, J. R. Ligand-Driven Wavelength-Tunable and Ultra-Broadband Infrared Luminescence in Single-Ion-Doped Transparent Hybrid Materials. *Adv. Funct. Mater.* **19**, 2081–2088 (2009).
27. Allix, M. *et al.* Considerable Improvement of Long-Persistent Luminescence in Germanium and Tin Substituted ZnGa₂O₄. *Chem. Mater.* **25**, 1600–1606 (2013).
28. Bai, G. X., Zhang, Y. & Hao, J. H. Chemical substitution-induced exceptional emitting-wavelength tuning in transition metal Ni²⁺-doped ferroelectric oxides with ultrabroadband near-infrared luminescence. *J. Mater. Chem. C* **2**, 4631–4635 (2014).
29. Li, Y. *et al.* Long persistent and photo-stimulated luminescence in Cr³⁺-doped Zn-Ga-Sn-O phosphors for deep and reproducible tissue imaging. *J. Mater. Chem. C* **2**, 2657–2663 (2014).
30. Premkumar, H. B. *et al.* Synthesis, characterization, EPR, photo and thermoluminescence properties of YAlO₃:Ni²⁺ nanophosphors. *J. Lumines* **135**, 105–112 (2013).
31. Azamat, D., Badalyan, A., Dejneka, A., Jastrabik, L. & Lančok, J. Electron spin-lattice relaxation of low-symmetry Ni²⁺ centers in LiF. *Appl. Phys. Lett.* **104**, 252902 (2014).

Acknowledgements

This work was financially supported by National Natural Science Foundation of China (Grants no. 51472091 and 51602063), Guangdong Natural Science Foundation (Grants no. 2014A030310444). This work was also supported by the Open Funds of the State Key Laboratory of High Field Laser Physics (Shanghai Institute of Optics and Fine Mechanics), and Luminescent Materials and Devices (South China University of Technology).

Author Contributions

J.R.Q. conceived and designed the experiments, and was responsible for the project planning. J.M.N. prepared the samples. J.M.N., Y.L. and S.S.L. investigated the spectroscopic properties. Q.Q.C., S.S.L. and Q.X. carried out the EPR study. J.M.N. wrote the manuscript. Y.L. and J.R.Q. checked the manuscript. All authors were involved in the discussion of the experimental results and reviewed the manuscript.

Additional Information

Supplementary information accompanies this paper at <https://doi.org/10.1038/s41598-017-12591-1>.

Competing Interests: The authors declare that they have no competing interests.

Publisher's note: Springer Nature remains neutral with regard to jurisdictional claims in published maps and institutional affiliations.



Open Access This article is licensed under a Creative Commons Attribution 4.0 International License, which permits use, sharing, adaptation, distribution and reproduction in any medium or format, as long as you give appropriate credit to the original author(s) and the source, provide a link to the Creative Commons license, and indicate if changes were made. The images or other third party material in this article are included in the article's Creative Commons license, unless indicated otherwise in a credit line to the material. If material is not included in the article's Creative Commons license and your intended use is not permitted by statutory regulation or exceeds the permitted use, you will need to obtain permission directly from the copyright holder. To view a copy of this license, visit <http://creativecommons.org/licenses/by/4.0/>.

© The Author(s) 2017